Hydrodynamic description of long-distance spin transport through noncollinear magnetization states: Role of dispersion, nonlinearity, and damping

Ezio Iacocca* and Mark A. Hoefer
Department of Applied Mathematics, University of Colorado, Boulder, Colorado 80309, USA

(Received 26 December 2018; published 3 May 2019)

Nonlocal compensation of magnetic damping by spin injection has been theoretically shown to establish dynamic, noncollinear magnetization states that carry spin currents over micrometer distances. Such states can be generically referred to as dissipative exchange flows (DEFs) because spatially diffusing spin currents are established by the mutual exchange torque exerted by neighboring spins. Analytical studies to date have been limited to the weak spin injection assumption whereby the equation of motion for the magnetization is mapped to hydrodynamic equations describing spin flow and then linearized. Here, we analytically and numerically study easy-plane ferromagnetic channels subject to spin injection of arbitrary strength at one extremum under a unified hydrodynamic framework. We find that DEFs generally exhibit a nonlinear profile along the channel accompanied by a nonlinear frequency tunability. At large injection strengths, we fully characterize a magnetization state we call a contact-soliton DEF (CS-DEF) composed of a stationary soliton at the injection site, which smoothly transitions into a DEF and exhibits a negative frequency tunability. The transition between a DEF and a CS-DEF occurs at the maximum precessional frequency and coincides with the Landau criterion: a subsonic to supersonic flow transition. Leveraging the hydraulic-electrical analogy, the current-voltage characteristics of a nonlinear DEF circuit are presented. Micromagnetic simulations of nanowires that include magnetocrystalline anisotropy and nonlocal dipole fields are in qualitative agreement with the analytical results. The magnetization states found here along with their characteristic profile and spectral features provide quantitative guidelines to pursue an experimental demonstration of DEFs in ferromagnetic materials and establish a unified description for long-distance spin transport.

DOI: 10.1103/PhysRevB.99.184402

I. INTRODUCTION

Noncollinear magnetization states represent a new paradigm for the transport of spin currents over micrometer distances [1–10]. A key concept that has enabled the study of these states is the hydrodynamic interpretation of magnetization dynamics, originally proposed in the seminal paper by Halperin and Hohenberg [11] in the context of the spin-wave dispersion relation for ferromagnets and antiferromagnets. Almost four decades later, a similar fluidlike interpretation was used to identify the relationship between an infinite-length, static noncollinear magnetization state in easy-plane ferromagnets and dissipationless spin transport [12]. These states were characterized by a homogeneous normal-to-plane magnetization and a winding in-plane magnetization. More importantly, energy dissipation via damping was inoperative because the texture was assumed to be static. As a consequence, the mutual exchange torque exerted by neighboring spins could be interpreted as an equilibrium spin current or exchange flow [13] that did not exhibit any dissipation.

While the prospect of a dissipationless spin current is tantalizing for novel energy-efficient applications [6,14–18], any magnetization dynamics are subject to dissipation via magnetic damping [19]. An example is the interface between a magnetic material and a spin sink that results in spin pumping [20]. To circumvent this problem, it is necessary to introduce energy into the system. From an analysis of the linearized hydrodynamic equations for a ferromagnet, it was predicted that spin injection at one extremum of a one-dimensional channel could sustain a dynamic, noncollinear magnetization state that was termed a *spin superfluid* [1,2]. Despite the fact that this is a solution to the linearized, long-wavelength hydrodynamic equations, the magnetization vector itself exhibits fully nonlinear spatiotemporal excursions in the form of complete planar rotations. As we will later show, this solution results from a linearized analysis of the equations of motion. The usage of the term superfluid was borrowed from a similarity between the order parameters that describe spin transport in a magnet and mass transport in, e.g., superfluid He^4 as well as the fact that the normal-to-plane magnetization is approximately constant along the channel, although very small. However, this so-called spin superfluid experiences energy loss via a spatially diffusing spin current, yet its uniform precessional frequency and linearly decaying spin-current profile present potential advantages to the exponential decay property of magnons. Similar states have been predicted for antiferromagnets [7,8,21,22], and their experimental evidence in such materials has been recently presented [9,23].

To avoid potential misinterpretation of the term "spin superfluid" and to emphasize the nonlocal compensation of damping along the channel by the exchange torque that originates from spin injection at the device boundary, we will refer

*ezio.iacocca@colorado.edu

to spin superfluids and their generalizations as *dissipative exchange flows, or DEFs* for short.

A more realistic setting for easy-plane ferromagnetic materials must consider the effect of in-plane anisotropy that breaks axial symmetry. For this configuration, it was shown that the hydrodynamic equations of motion map to a damped sine-Gordon equation, with a nonlinear term proportional to the in-plane anisotropy strength [1,5]. Because of the broken symmetry imposed by in-plane anisotropy, the structure of a DEF is that of a translating train of Néel domain walls or a soliton lattice with the same chirality and whose interwall spacing increases as each domain wall propagates from the spin injection edge to the opposite free spin edge. In the limit of vanishing anisotropy, the train of domain walls smooths into a sinusoidal profile, equivalent to the previously studied, axially symmetric case [1,2].

The most striking feature of a DEF is that its spatial structure and coherent precessional frequency depend on the length of the channel. It is a solution to a boundary-value problem whereby the channel's extrema are subject to spin injection and spin pumping or free spin boundary conditions. As a result, these solutions exhibit peculiar characteristics of technological relevance, [5], i.e., the spin injection threshold is proportional to the square root of the in-plane anisotropy field for long channels, and the homogeneous frequency is inversely proportional to damping and the channel's length. For comparison, spin waves [24] excited on a homogeneous magnetization background exhibit a spin-injection threshold that is proportional to damping, a frequency proportional to both spin injection and the magnet's internal field, and an exponential decay rate that is proportional to damping. The exponential decay of spin waves imposes the ultimate limitation on their propagation length and coherent spin transport, although detection at micrometer length scales has been achieved in low-damping materials such as YIG [25], amorphous YIG [26], and haematite [27].

The analytical predictions and characteristics of DEFs are promising for long-distance spin transport. However, the required spin injection has emerged as a practical barrier for their experimental realization. In recent experimental studies, spin injection was realized from quantum Hall edge states in antiferromagnetic graphene [9] and the spin-Hall effect in Pt [23]. A recent numerical study proposes an alternative spin-injection mechanism based on the spin-transfer torque effect [28,29], which excites magnetization precession [5]. This method allows for large spin-injection magnitudes, breaking the weak injection assumption that has been analytically assumed to date [1,2]. Signatures of distinct nonlinear, dispersive dynamics exhibiting solitonic features were observed in micromagnetic simulations that include nonlocal dipole fields [5]. More recently, micromagnetic simulations that incorporate spin-transfer torque along a confined, central strip of a ferromagnet have similarly shown evidence of strongly nonlinear features including a soliton nucleated at the injection site in the large injection regime, termed a "soliton screened spin superfluid" [10].

While the numerical studies to date by a variety of groups unambiguously demonstrate that long-range spin transport can in principle be achieved with noncollinear magnetization states in magnetic materials, an analysis that incorporates short-wavelength exchange dispersion and large-amplitude nonlinearities due to anisotropy—such as those necessarily present for the existence of a soliton—as well as a description of the effect of damping on spin flows is lacking. Here, we provide a unified analytical framework in the context of a dispersive hydrodynamic (DH) formulation of magnetization dynamics [3,4]. This formulation is an exact transformation of the Landau-Lifshitz equation and, therefore, captures the essential physics that are relevant to describe fully nonlinear, noncollinear magnetization states: exchange, anisotropy, and damping.

The DH formulation gives rise to two equations of motion for a longitudinal spin density and its associated fluid velocity that are analogous to the Navier-Stokes' mass and momentum equations for a compressible fluid [3,4]. From a fluid perspective, exchange, anisotropy, and damping give rise to dispersion, nonlinearity, and viscosity, respectively. In contrast to typical fluids, the equivalent magnetic fluid exhibits a nonconserved density, i.e., the mass can be lost. Therefore, noncollinear magnetization states—DEFs—can be interpreted as forced fluid flows that compensate the density and viscous losses manifesting in a profile that balances dispersion and nonlinearity.

In this paper, we find that DEFs are generally characterized by a nonlinear profile in both density and fluid velocity. In the weak spin injection regime, the DH equations reduce to the forced diffusion equation and lead to a linear DEF solution that is equivalent to a spin superfluid [1,2]. Using boundary-layer theory in the strong spin injection regime, we find a dynamical state characterized by the nucleation of a stationary soliton at the injection site that smoothly transitions into a nonlinear DEF. We term this dynamical solution as a contact soliton DEF, or CS-DEF, which is an analytical representation of the numerically identified soliton screened spin superfluid [10]. From a hydrodynamic perspective, the soliton nucleated at the injection site occurs precisely when the injection crosses the subsonic to supersonic flow boundary, equivalent to the Landau criterion [3,4]. Moreover, the transition between a DEF and a CS-DEF corresponds to the maximum precessional frequency achieved by spin injection, setting an upper bound to the efficiency of DEF-mediated spin transport. Thus, further spin injection enhances the coherent, superfluid-like soliton at the expense of larger spin transport, which is in sharp contrast to classical fluids where strong channel flows are subject to drag at the boundaries that, above a critical Reynolds number, develop into an incoherent, turbulent state [30].

The presented results pertain to an ideal geometry whereby the magnetic material is defect-free and the boundaries are perfect spin-current sources and drains. Deviations from these conditions may result in qualitative changes to the presented solutions, including instabilities. Defects in the magnetic material can result in magnetic topological defects that destabilize the DEFs, e.g., vortex-antivortex pairs [4] or phase slips [1,16,31]. Nonideal boundaries can be incorporated by utilizing mixed (Robin) boundary conditions from a circuit formalism that includes spin pumping [2]. In the case of strong injection, recent numerical results suggest that such boundaries can induce an instability in the DEF to CS-DEF crossover region [10]. Our results aim to provide the analytical basis to further study these effects in more detail.

Our analytical study also indicates that, for the physically relevant case of magnetic materials with low damping, DEFs can be interpreted as an adiabatic spatial evolution of conservative dynamic solutions, previously termed uniform hydrodynamic states (UHSs) [3] in order to highlight their nondissipative, flowing character. DEF magnetization states sustained in channels subject to subsonic spin-injection conditions can be conveniently represented as curves of constant frequency in the UHS phase space of spin density and fluid velocity. From an applications perspective, the fluid interpretation also lends itself to a circuit analogy, from which we can define the current-voltage (I-V) characteristics of the coherent states studied here. Micromagnetic simulations support the analytical results even in the presence of in-plane anisotropy and nonlocal dipole fields in a thin film.

The remainder of the paper is organized as follows. In Sec. II, we summarize the dispersive hydrodynamic formulation and the main features of uniform hydrodynamic states. In Sec. III, we introduce the boundary-value problem that describes a channel subject to spin injection at one extremum, and we derive analytical expressions for linear DEFs, DEFs, and CS-DEFs. In the same section, we study the DEF to CS-DEF transition in the context of a subsonic to supersonic flow transition. In Sec. IV, we establish that the hydrodynamic states sustained in channels realize a nonlinear resistor in the hydraulic analogy of electrical circuits. Micromagnetic simulations of nanowires incorporating STT as a spin-injection mechanism, in-plane magnetocrystalline anisotropy, and nonlocal dipole fields are discussed in Sec. V. Finally, we provide our concluding remarks in Sec. VI.

II. DISPERSIVE HYDRODYNAMIC FORMULATION AND UNIFORM HYDRODYNAMIC STATES

Magnetization dynamics in a continuum approximation can be described by the Landau-Lifshitz (LL) equation

$$\partial_t \mathbf{m} = -\mathbf{m}\times\mathbf{h}_{\mathrm{eff}} - \alpha\mathbf{m}\times\mathbf{m}\times\mathbf{h}_{\mathrm{eff}}, \tag{1a}$$

$$\mathbf{h}_{\mathrm{eff}} = \underbrace{\Delta\mathbf{m}}_{\text{exchange}} - \underbrace{m_z\hat{\mathbf{z}}}_{\text{local dipole}}, \tag{1b}$$

where $\mathbf{m} = (m_x, m_y, m_z)$ is the magnetization vector normalized to the saturation magnetization M_s, α is the phenomenological Gilbert damping parameter, and $\mathbf{h}_{\mathrm{eff}}$ is an effective field, normalized by M_s, that incorporates the exchange and local (zero-thickness) dipole field as a minimal model for dispersion and nonlinearity, respectively. The dimensionless form of Eq. (1a) is achieved by scaling time by $|\gamma|\mu_0 M_s$ and space by $\lambda_{\mathrm{ex}}^{-1}$, where γ is the gyromagnetic ratio, μ_0 is the vacuum permeability, and λ_{ex} is the exchange length. A dispersive hydrodynamic representation of Eqs. (1a) and (1b) can be achieved by mapping the magnetization vector into hydrodynamic variables [3–5], namely a longitudinal spin density $n = m_z$ and a fluid velocity $\mathbf{u} = -\nabla\Phi = -\nabla \arctan(m_y/m_x)$. In this work, we are interested in effectively one-dimensional dynamics along a channel whose length is oriented in the $\hat{\mathbf{x}}$ direction. Therefore, the fluid velocity can be written as a scalar quantity $u = \mathbf{u}\cdot\hat{\mathbf{x}}$ and the spatial derivatives taken only along $\hat{\mathbf{x}}$. The resulting dispersive hydrodynamic equations are

$$\partial_t n = (1+\alpha^2)\partial_x[(1-n^2)u] + \alpha(1-n^2)\partial_t\Phi, \tag{2a}$$

$$\partial_t\Phi = -(1-u^2)n + \frac{\partial_{xx}n}{1-n^2} + \frac{n(\partial_x n)^2}{(1-n^2)^2} - \frac{\alpha}{1-n^2}\partial_x[(1-n^2)u]. \tag{2b}$$

The simplest solutions to Eqs. (2a) and (2b) are spin-density waves (SDWs). These are static ($\partial_t\Phi = 0$), textured magnetization states parametrized by a constant density and fluid velocity, (n_0, u_0). SDWs are magnetization states that support dissipationless spin transport [12]. A dynamic SDW can only be obtained as a transient state or in the conservative limit, where $\alpha = 0$ and $\partial_t\Phi \neq 0$. We refer to this state as a uniform hydrodynamic state (UHS). For both SDWs and UHSs, the density is limited by its deviation from the magnetization's unit sphere poles ($n = \pm 1$ corresponds to vacuum) while the fluid velocity is an unbounded quantity. However, it was shown in Ref. [3] that modulational instability [32] (the exponential growth of perturbations) ensues when $|u_0| > 1$, i.e., for SDWs and UHSs with subexchange length, in-plane magnetization rotation wavelengths. Therefore, modulationally stable SDWs and UHSs are defined in the phase space spanned by $|n_0| < 1$ and $|u_0| < 1$. UHSs exhibit a precessional frequency given by

$$\Omega_0 = \partial_t\Phi = -\left(1-u_0^2\right)n_0, \tag{3}$$

obtained directly from Eq. (2b). The negative sign of the frequency for $n_0 > 0$ indicates that the precession is clockwise about the $\hat{\mathbf{z}}$ direction. It is important to emphasize that UHSs are dynamic, textured magnetization states. This is markedly different from small-amplitude perturbations about a homogeneous state that are typically associated with spin waves. Interestingly, UHSs support small-amplitude perturbations that exhibit a dispersion relation that is nonreciprocal for $n \neq 0$ [3,4]. This nonreciprocity leads to conditions in which long-wavelength perturbations can propagate in either two directions or one direction with respect to the UHS fluid velocity u_0 and can be hydrodynamically interpreted as subsonic or supersonic flow, respectively. The transition between subsonic and supersonic flow is known as the sonic curve. For UHSs, the sonic curve is given by

$$|u_0| = \sqrt{\frac{1-n_0^2}{1+3n_0^2}}, \tag{4}$$

and it is shown in Fig. 1 by a solid black curve in the UHS phase space. Equation (4) is formally equivalent to the Landau criterion for superfluidity in the limit of perpendicularly magnetized easy-plane ferromagnets [4] and for linear DEFs or spin superfluids [8]. Isofrequency contours determined from Eq. (3) are shown by dashed black curves. As we will demonstrate below, the UHS phase space provides information regarding the form of dynamic magnetization states in ferromagnetic channels sustained by spin injection.

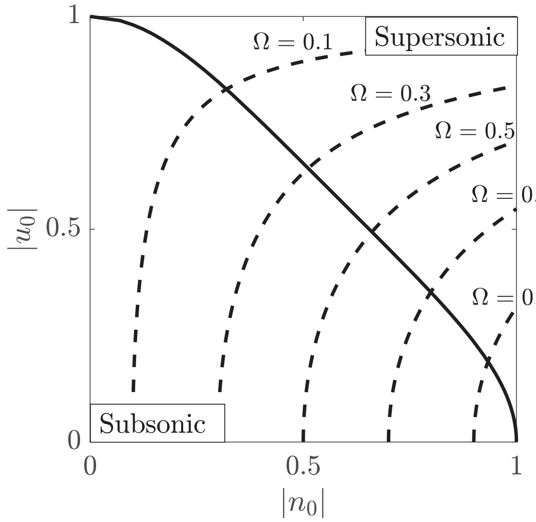

FIG. 1. UHS phase space for density $|n_0| \leqslant 1$ and fluid velocity $|u_0| \leqslant 1$. The sonic curve that separates the subsonic and supersonic regions is shown by a solid black curve. The dashed black curves represent isofrequency contours, labeled by the corresponding frequency.

III. BOUNDARY-VALUE PROBLEM FOR EASY-PLANE FERROMAGNETIC CHANNELS

The steady magnetization states sustained by spin injection can be analytically obtained by solving Eqs. (2a) and (2b) subject to appropriate boundary conditions (BCs). For this, we consider a channel of length L and introduce spin injection at $x = 0$ and free spin boundary conditions at $x = L$. For simplicity, we disregard spin pumping [2], but our analysis is sufficiently general that more complex BCs that incorporate metal/magnetic interfacial effects could be studied in a similar manner.

We seek steady, precessional solutions to

$$0 = (1+\alpha^2)\frac{d}{dx}[(1-n^2)u] + \alpha(1-n^2)\Omega, \tag{5a}$$

$$\Omega = -(1-u^2)n + \frac{1}{1-n^2}\frac{d^2n}{dx^2} + \frac{n}{(1-n^2)^2}\left(\frac{dn}{dx}\right)^2 - \frac{\alpha}{1-n^2}\frac{d}{dx}[(1-n^2)u] \tag{5b}$$

with BCs,

$$\frac{dn}{dx}(0) = 0, \quad \frac{dn}{dx}(L) = 0, \tag{6a}$$

$$u(0) = \bar{u}, \quad u(L) = 0, \tag{6b}$$

where $\bar{u}$ is proportional to the injected spin current [5]. These boundary conditions are enforced upon $n = n(x)$, $u = u(x)$ by introducing the homogeneous precessional frequency $\Omega = \partial_t\Phi$. Below, we find solutions of this boundary-value problem (BVP) with nonlinearity, dispersion, and damping. A more detailed, mathematical analysis leading to these approximate solutions is provided in the Appendix.

A. Linear DEFs

We begin our analysis by revisiting the weak spin-injection regime $0 < |\bar{u}| \ll \min(1, \alpha L)$, first presented in [1,2]. For this, we assume that u is small and n is constant in Eqs. (5a) and (5b), so that the linearized equations are

$$\alpha\tilde{\Omega} = -\frac{du}{dx}, \tag{7a}$$

$$\tilde{\Omega} = -n, \tag{7b}$$

where $\tilde{\Omega} = \Omega/(1+\alpha^2)$.

Noting that $u = -\partial_x\Phi$ and $\Omega = \partial_t\Phi$, we can rewrite Eqs. (7) as the diffusion equation

$$\frac{\alpha}{1+\alpha^2}\partial_t\Phi = \partial_{xx}\Phi, \tag{8}$$

subject to the boundary conditions

$$\partial_x\Phi(0) = -\bar{u}, \quad \partial_x\Phi(L) = 0. \tag{9}$$

For weak damping, $1+\alpha^2 \sim 1$, Eq. (8) is the linearized hydrodynamic diffusion equation for easy-plane ferromagnets from previous studies [1,2]. By direct integration, Eq. (8), subject to Eq. (9), exhibits the linear DEF solution,

$$u_{l\mathrm{DEF}} = \bar{u}\left(1 - \frac{x}{L}\right), \quad \tilde{\Omega}_{l\mathrm{DEF}} = -n_{l\mathrm{DEF}} = \frac{\bar{u}}{\alpha L}, \tag{10}$$

which exhibits a linear decay profile in the fluid velocity, which corresponds to the algebraic diffusion of spin current across the channel. Importantly, this approximate solution exhibits a spatially homogeneous frequency and density, with no assumptions on the magnitudes of nonzero damping nor the channel length L. See Appendix A 1 for additional details.

It is important to emphasize that damping plays a fundamental role in the stabilization of the linear DEF solution. It is for this reason that we refer to the solution as a dissipative exchange flow. In fact, in the conservative case in which $\alpha = 0$, the solution to Eq. (7a) ($u = \text{const}$) cannot satisfy both boundary conditions (9).

B. Nonlinear DEFs

We now consider nonlinear but spatially smooth solutions, i.e., slowly varying relative to the exchange length for a long channel $L \gg 1$. Consequently, the dispersive terms in Eq. (2b) can be neglected [both d^2n/dx^2 and $(dn/dx)^2$]. Upon simple algebraic manipulation, Eqs. (5a) and (5b) reduce to

$$\alpha(1-n^2)\tilde{\Omega} = -\frac{d}{dx}[(1-n^2)u], \tag{11a}$$

$$\tilde{\Omega} = -(1-u^2)n. \tag{11b}$$

Inserting n from Eq. (11b) into (11a) leads, after some algebra, to the differential equation

$$\alpha\tilde{\Omega} = \frac{du}{dx}\left[\frac{(\alpha\tilde{\Omega}u)^2}{(1-u^2)(u^4-2u^2+1-\tilde{\Omega}^2)} - 1\right], \tag{12}$$

which relates the fluid velocity to the precessional frequency. By integration, we obtain an implicit equation for the fluid

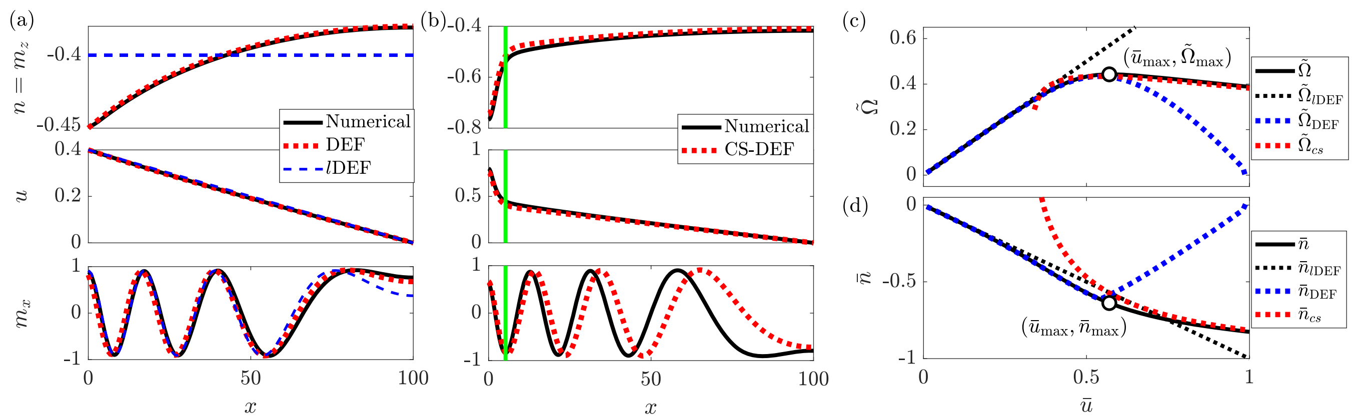

FIG. 2. Magnetization states in a channel of length $L = 100$ and $\alpha = 0.01$ subject to the injection $\bar{u}$ at the left edge, $x = 0$. In (a) and (b), the panels represent the density n, fluid velocity u, and m_x magnetization vectorial component at an instant of time. (a) For the injection $\bar{u} = 0.4$, the numerical solution shown by solid black curves is in excellent agreement with a DEF shown by dashed red curves. For comparison, the corresponding linear DEF solution is shown by dashed blue curves. (b) For the injection $\bar{u} = 0.8$, the numerical solution shown by solid black curves is in good agreement with a CS-DEF shown by dashed red curves. The solid green line indicates the boundary-layer length where the soliton is established. (c) Precessional frequency as a function of injection for a linear DEF (dashed black line), numerical solution of the BVP (solid black curve), DEF (dashed blue curve), and CS-DEF (dashed red curve). The numerical maximum $\tilde{\Omega}_{\max} = 0.44$ is found at $\bar{u} = 0.57$. (d) Density at the injection site, $\bar{n} = n(0)$, using the same color codes as (c).

velocity (see Appendix A 2),

$$\alpha L\tilde{\Omega}_{\rm DEF}\left(1-\frac{x}{L}\right) = u_{\rm DEF} + 4\tanh^{-1}(u_{\rm DEF}) - 2\mathcal{N}^{-}(u_{\rm DEF},\tilde{\Omega}_{\rm DEF}) - 2\mathcal{N}^{+}(u_{\rm DEF},\tilde{\Omega}_{\rm DEF}), \quad (13)$$

where

$$\mathcal{N}^{\pm}(\kappa,\omega) = \sqrt{1\pm\omega}\,\tanh^{-1}\left(\frac{\kappa}{\sqrt{1\pm\omega}}\right). \quad (14)$$

The precessional frequency is obtained by evaluating Eq. (13) at $x = 0$, where $u_{\rm DEF}(0) = \bar{u}$, implying the equation for the DEF's frequency,

$$\alpha L\tilde{\Omega}_{\rm DEF} = \bar{u} + 4\tanh^{-1}(\bar{u}) - 2[\mathcal{N}^{-}(\bar{u},\tilde{\Omega}_{\rm DEF}) + \mathcal{N}^{+}(\bar{u},\tilde{\Omega}_{\rm DEF})], \quad (15)$$

while the density is obtained directly from Eq. (11b) as

$$n_{\rm DEF} = -\frac{\tilde{\Omega}_{\rm DEF}}{1-u_{\rm DEF}^2}. \quad (16)$$

Equations (13), (15), and (16) indicate that the DEF's spatial profile is, in general, nonlinear and the frequency is a nonlinear function of the spin injection $\bar{u}$. A numerical solution for a nonlinear DEF is shown by dashed red curves in Fig. 2(a) for the injection $\bar{u} = 0.4$, a channel of length $L = 100$, and $\alpha = 0.01$. The top and center panels show the hydrodynamic variables $n(x)$ and $u(x)$, respectively, while the bottom panel shows the $\hat{\mathbf{x}}$ magnetization component, $m_x(x,t) = \sqrt{1-n(x)^2}\cos\Phi(x)$, at a given instant of time (recall that $\partial_t\Phi \neq 0$). Excellent agreement is obtained between the analytical solution and the numerical solution of the full BVP in Eqs. (2a), (2b), (6a), and (6b), shown by solid black curves. The BVP is numerically solved by a collocation method (MATLAB's bvp5c).

An important consequence of the DEF nonlinear profile is the concomitant precessional frequency that is a nonlinear function of the injection, $\bar{u}$, shown by a dashed blue curve in Fig. 2(c). The frequency obtained by solving the full BVP is shown by a solid black curve. Excellent agreement with Eq. (15) is found up to the maximum frequency $\tilde{\Omega}_{\max} = 0.44$ at $\bar{u}_{\max} = 0.57$, indicated by a black circle. For $\bar{u} > \bar{u}_{\max}$, the nonlinear solution no longer describes the frequency dependence. The density at the injection site, equivalent to the magnetization tilt due to spin injection, is shown in Fig. 2(d). Similar to the precessional frequency, a good quantitative agreement between the numerical solution (solid black curve) and the DEF solution (dashed blue curve) is observed up to $\bar{u}_{\max} = 0.57$, where $\bar{n}_{\max} = -0.64$. As we show below, these qualitative changes indicate the initiation of supersonic flow and of a stationary soliton.

The linear DEF solution can be obtained from the nonlinear DEF solution in the weak injection regime. For this, we note that $\tanh^{-1}(\kappa) \approx \kappa$ and $\mathcal{N}^{\pm}(\kappa,\omega) \approx \kappa$ for small κ. Introducing these approximations in Eqs. (13), (15), and (16) leads to Eq. (10).

The linear DEF approximation is shown by dashed blue curves in Fig. 2(a) for the same parameters as the DEF and numerical solutions. It is interesting that while the difference between the linear and nonlinear spatial profiles for the fluid velocity (middle panel) is imperceptible, the density in a linear approximation does not conform to the spatial profile. A consequence is that the linear DEF frequency tunability is likewise a linear function of injection and quantitatively agrees with the nonlinear solution up to $\bar{u} \approx 0.3$ for $L = 100$ and $\alpha = 0.01$, shown in Fig. 2(c) by a dashed black line.

C. Contact soliton DEFs

The qualitative change in the frequency dependence observed in Fig. 2(c) is an indication that the inclusion of nonlinearity and lowest-order dispersion is not sufficient to describe DEF solutions sustained at an arbitrary injection strength. In such a regime, higher-order dispersive terms must be taken into account in Eqs. (5a) and (5b). An analytical methodology for this task is boundary-layer theory [33]. This method allows one to separate the system into regimes dominated by different physics that can be asymptotically matched. Below we outline the most important features and results obtained from the calculation. Details can be found in Appendix A 3.

For Eqs. (5a) and (5b) subject to the BCs (6a) and (6b), it is possible to identify two regimes. Close to the left edge subject to strong injection, the spatial profile of the solution can vary rapidly. In other words, we assume that dispersion dominates over damping. Asymptotically, this is equivalent to an expansion with small damping while considering short spatial variations, as discussed in the Appendix. We refer to this region as the inner region. Far from the left edge, we assume that the spatial profile of the solution varies slowly, so that damping dominates over dispersion. We refer to this region as the outer region. A matching condition is invoked to obtain a smooth solution across both regions. Mathematically, this is achieved by introducing BCs for the inner region,

$$\frac{d}{dx}n_{\text{in}}(0) = 0, \quad \lim_{x\to\infty} n_{\text{in}}(x) = n_\infty, \tag{17a}$$

$$u_{\text{in}}(0) = \bar{u}, \quad \lim_{x\to\infty} u_{\text{in}}(x) = u_\infty, \tag{17b}$$

and the outer region,

$$\lim_{x\to 0} n_{\text{out}}(x) = n_\infty, \quad \frac{d}{dx}n_{\text{out}}(L) = 0, \tag{18a}$$

$$\lim_{x\to 0} u_{\text{out}}(x) = u_\infty, \quad u_{\text{out}}(L) = 0, \tag{18b}$$

where n_∞ and u_∞ are matching parameters to be determined.

The equations of motion for the inner region are dominated by dispersion so that the dissipative terms are neglected,

$$0 = \frac{d}{dx}[(1-n^2)u], \tag{19a}$$

$$\tilde{\Omega} = -(1-u^2)n + \frac{1}{1-n^2}\frac{d^2n}{dx^2} + \frac{n}{(1-n^2)^2}\left(\frac{dn}{dx}\right)^2. \tag{19b}$$

The solution of this system of differential equations involves a series of steps detailed in Appendix A 3. Ultimately, Eqs. (19a) and (19b) can be integrated to obtain the soliton solution, e.g., see Ref. [34],

$$n_{\text{in}} = \frac{a\nu_1 \tanh^2(\theta x) + \nu_2(n_\infty - a)}{a\tanh^2(\theta x) + \nu_2}, \tag{20a}$$

$$u_{\text{in}} = u_\infty \frac{1-n_\infty^2}{1-n_{\text{in}}^2}, \tag{20b}$$

$$\tilde{\Omega}_{\text{in}} = -n_\infty(1-u_\infty^2), \tag{20c}$$

with two free parameters: n_∞, u_∞. The coefficients ν_1, ν_2, θ, and a are given in Appendix A 3, and all BCs in Eqs. (17a) and (17b) were used. In other words, Eqs. (20a) and (20b) describe, respectively, solitons of density amplitude a on a nonzero density background n_∞ and fluid velocity background u_∞.

In contrast, the slowly varying outer region is dominated by damping, leading to Eqs. (11a) and (11b) with DEF solutions given by Eqs. (13) and (16) that we term u_{out} and n_{out}, respectively. We note that this solution is obtained by evaluating the BCs of Eqs. (18a) and (18b) at $x = L$, yielding a two-parameter family of solutions,

$$n_{\text{out}} = -\frac{\tilde{\Omega}_{\text{out}}}{1-u_{\text{out}}^2}, \tag{21a}$$

$$\alpha L\tilde{\Omega}_{\text{out}}\left(1-\frac{x}{L}\right) = u_{\text{out}} + 4\tanh^{-1}(u_{\text{out}}) - 2[\mathcal{N}^-(u_{\text{out}},\tilde{\Omega}_{\text{out}}) + \mathcal{N}^+(u_{\text{out}},\tilde{\Omega}_{\text{out}})]. \tag{21b}$$

To apply boundary-layer theory, the inner and outer solutions must asymptotically match and exhibit a single precessional frequency $\tilde{\Omega}_{\text{cs}} = \tilde{\Omega}_{\text{in}} = \tilde{\Omega}_{\text{out}}$. For the left edge of the channel subject to spin injection, we evaluate the inner region solution, Eqs. (20a) and (20b) at $x = 0$, to obtain

$$\bar{u} = u_\infty \frac{1-n_\infty^2}{1-(n_\infty - a)^2}. \tag{22}$$

Then, we evaluate the matching conditions applied to the outer solution, Eqs. (18a) and (18b), by evaluating Eqs. (21a) and (21b) at $x = 0$ and identifying $u_{\text{out}}(0) = u_\infty$ and $n_{\text{out}}(0) = n_\infty$.

We now have all the ingredients to construct a uniformly valid solution along the length L of the channel. Such a solution can be written as

$$u_{\text{cs}}(x) = u_{\text{in}}(x) + u_{\text{DEF}}(x) - u_\infty, \tag{23a}$$

$$n_{\text{cs}}(x) = n_{\text{in}}(x) + n_{\text{DEF}}(x) - n_\infty, \tag{23b}$$

which describes a soliton located at the injection site smoothly connected to a nonlinear DEF. We call this solution a contact soliton dissipative exchange flow (CS-DEF).

A CS-DEF is shown by dashed red curves in Fig. 2(b) for the injection $\bar{u} = 0.8$, a channel of length $L = 100$, and $\alpha = 0.01$. The numerical solution of the full BVP is shown by solid black curves and it is in excellent quantitative agreement with the boundary-layer approach. The frequency dependence on the injection $\bar{u}$ is shown by a dashed red curve in Fig. 2(c). In contrast to the DEF frequency tunability, the CS-DEF precessional frequency is decreasing with $\bar{u}$. Additionally, we observe that the numerically obtained frequency tunability (solid black line) approaches the CS-DEF frequency above $\bar{u}_{\text{max}}$. A similar behavior is observed for the density at the injection site, shown in Fig. 2(d) by the dashed red curve. These observations indicate that the full solution profile as a function of injection $\bar{u}$ transitions from a DEF into a CS-DEF. In the following section, we investigate this transition and its hydrodynamic interpretation.

Qualitatively, CS-DEFs are similar to the soliton screened spin superfluid recently calculated in micromagnetic simulations [10]. An important difference is that our free-spin boundary conditions model a perfect spin sink so that magnon reflections are inhibited.

D. DEF to CS-DEF transition

In the previous section, a transition from a DEF into a CS-DEF was evidenced by a qualitative change in the frequency tunability to injection. In particular, it is observed in

Fig. 2(c) that the full numerical solution (solid black curve) approaches the DEF and CS-DEF frequency tunabilities in the small and large injection limits, respectively. Whereas a first-order transition is not observed, it is insightful to find an analytical expression for a practical observable, such as the maximum precessional frequency, $\tilde{\Omega}_{\rm max}$. For this, we can utilize the implicit equation for a DEF fluid velocity profile, Eq. (15), to take the derivative with respect to u and equate $d/d\bar{u}(\tilde{\Omega}_{\rm DEF}) = 0$. Because Eq. (15) is implicit, the maximum frequency will be an implicit equation as well. Utilizing Eq. (16), we can eliminate $\tilde{\Omega}_{\rm DEF}$ and, after some algebra, we obtain the injection at maximum frequency, $\bar{u}_{\rm max}$, that depends on the input density at maximum frequency, $\bar{n}_{\rm max}$, according to

$$|\bar{u}_{\rm max}| = \sqrt{\frac{1-\bar{n}_{\rm max}^2}{1+3\bar{n}_{\rm max}^2}}. \tag{24}$$

Interestingly, this is precisely the sonic curve, Eq. (3). This relation is a central result of this work. There are three physical implications of Eq. (24). First, the relation bounds the phase space for DEFs to the UHS subsonic regime, below the solid curve in Fig. 1. Second, it suggests that DEFs can be interpreted as the adiabatic spatial evolution through a family of UHSs parametrized by spatially dependent densities and fluid velocities. An adiabatic interpretation is valid as long as $\alpha \ll 1$, which is physically true for magnetic materials of interest. Third, exceeding $\bar{u}_{\rm max}$ implies supersonic flow and coincides with the development of a soliton at the injection site.

A consequence of the adiabatic interpretation of DEF solutions is that the solution's profiles can be visualized within UHS phase space. In Fig. 3(a), we show numerical solutions of the BVP for $L = 100$ and $\alpha = 0.01$ by solid blue curves. The input conditions for each case are marked by blue circles. The solid and dashed gray curves represent the UHS sonic curve and isofrequency contours, respectively. We observe that the density and fluid velocity of several DEFs lie on UHS isofrequency contours. When the injection and its corresponding density enter the supersonic regime, CS-DEFs ensue and the adiabatic interpretation breaks down. Numerical solutions for CS-DEFs visualized in the UHS phase space are shown by dashed red curves in Fig. 3(a) where the input conditions are marked by red circles. Close to the injection site, where the soliton is established, the profile does not follow the isofrequency contours. However, once the sonic curve is crossed, the profile transitions into that of a DEF and spatially evolves adiabatically along an isofrequency contour in UHS phase space.

From a hydrodynamic perspective, the UHS phase-space visualization emphasizes a remarkable quality of CS-DEFs. In classical fluids, high-speed flow with boundaries is subject to instabilities that result in turbulent flow, i.e., characteristic spatial scales become smaller downstream. Instead, the soliton established at the injection site is a coherent structure that expands the spatial scales to a slowly varying DEF, precluding turbulence and ultimately establishing a slower subsonic flow. This feature is possible at the expense of reducing the homogeneous precessional frequency and, consequently, the magnitude of spin currents pumped into a reservoir located,

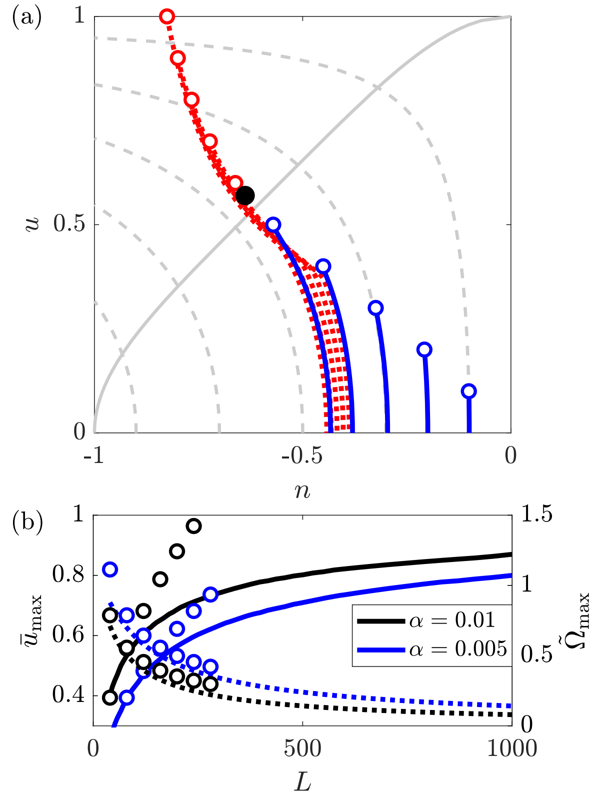

FIG. 3. (a) DEFs (solid blue curves) and CS-DEFs (dashed red curves) represented in the UHS phase space. The sonic curve and isofrequency contours are shown by a solid and dashed gray curve, respectively. The DEFs lie on the isofrequency contours, in agreement with an adiabatic interpretation. CS-DEFs behave markedly differently when the parameters are in the supersonic regime. The density and injection at the frequency maximum for $L = 100$, $(\bar{n}_{\rm max}, \bar{u}_{\rm max})$, is shown by a black circle. (b) Injection (left axis, solid curves) and frequency (right axis, dashed curves) at which a DEF transitions into a CS-DEF as a function of the channel length L and setting $\alpha = 0.01$ (black) and $\alpha = 0.005$ (blue). Analytical estimates obtained from an asymptotic expansion in $\bar{u}$ of the nonlinear DEF solution are shown by circles with the color code described above.

e.g., at the right edge of the channel. It must be noted that supersonic conditions close to the left edge of the channel make this region susceptible to instabilities via phase slips [1] or vortex-antivortex pair creation [4] at defect sites. A detailed study of CS-DEF instabilities as well as the conditions that trigger such instabilities is a separate study.

As discussed above, the distinction between DEFs and CS-DEFs from a hydrodynamic perspective can be linked to the flow conditions at the injection site. However, Eq. (24) is expressed as a function of $\bar{n}_{\rm max}$, which is an *a priori* unknown quantity that is determined by solving for a DEF. In other words, Eq. (24) cannot predict which isofrequency contour in Fig. 3(a) will be followed by a DEF given only the injection $\bar{u}$. A practical consequence is that the actual maximum injection and precessional frequency will depend on L and α. By numerically solving the BVP as a function of L, we find the maximum injection $\bar{u}_{\rm max}$ and frequency $\tilde{\Omega}_{\rm max}$ shown, respectively, by solid and dashed curves in Fig. 3(b) for $\alpha = 0.01$ (blue) and $\alpha = 0.005$ (black). The density and injection at the frequency maximum for $L = 100$, $(\bar{n}_{\max}, \bar{u}_{\max})$, is shown by a black circle in Fig. 3(a). These results have a clear physical interpretation. For short channels, the problem limits to a local balance between injection and damping. Therefore, the energy introduced into the system is primarily invested in spin precession. In the opposite limit of long channels, the energy is mainly invested in establishing a DEF to compensate damping nonlocally, and $\bar{u}_{\max}$ is large.

Analytical expressions for both $\bar{u}_{\max}$ and $\tilde{\Omega}_{\max}$ can be obtained from the asymptotic expansion in $\bar{u}$ of the nonlinear DEF solution, written in Appendix A 2. Following the same procedure as outlined above, we obtain

$$\bar{u}_{\max} \approx \left(\frac{3}{20}\right)^{1/4}\sqrt{\alpha L} \approx 0.6223\sqrt{\alpha L}, \tag{25a}$$

$$\tilde{\Omega}_{\max} \approx \left(\frac{3}{20}\right)^{1/4}\frac{4}{5}\frac{1}{\sqrt{\alpha L}} \approx 0.4979\frac{1}{\sqrt{\alpha L}}. \tag{25b}$$

These solutions are valid for small αL. A comparison to our analytical results is shown in Fig. 3(b) with black and blue circles for, respectively, $\bar{u}_{\max}$ and $\tilde{\Omega}_{\max}$. For the typical small values of α, good agreement is observed up to $L \approx 200$.

We emphasize that neither in-plane anisotropy nor nonlocal dipole fields have been included in the analysis. For short channels, these fields will most likely change the easy-axis direction, which could destroy the onset of magnetization textures. However, for long channels, it has been shown that such symmetry-breaking fields primarily introduce a threshold for the onset of DEFs [5]. This implies that the large injections required to trigger a transition into a CS-DEF will be negligibly affected, as recently observed by simulations [10]. In Sec. V, we explore this transition by micromagnetic simulations in nanowires where the injection is parametrized by STT.

E. Boundary-layer width

The CS-DEF solution presented in Eqs. (23a) and (23b) was obtained by separating the problem into two distinct regions—inner and outer—followed by asymptotic matching. A relevant parameter to identify is the width of the solitonic inner region as a function of the injection $\bar{u}$.

The boundary-layer width is linked to the soliton width, whose profile is given in Eq. (20a). Because solitons decay exponentially, its width can be estimated from the profile's half-width at half-maximum. We will use this metric to estimate the boundary-layer width, l.

The soliton solution Eq. (20a) has an amplitude a over a background n_∞. Therefore, the half-width at half-maximum can be calculated by imposing $n_{\text{in}}(x = l) = -a/2 + n_\infty$. After some algebra, we obtain the implicit equation for l,

$$\tanh^2(\theta l) = \frac{\nu_2}{2(\nu_1 - n_\infty) + a}, \tag{26}$$

which can be solved numerically as a function of $\bar{u}$ given the boundary and matching conditions (21a), (21b), and (22). Figure 4 depicts the boundary-layer width as a function of $\bar{u}$ larger than $\bar{u}_{\max}$, where the CS-DEF solution occurs in a channel of length $L = 100$. We observe that the boundary-layer width decreases, i.e., the soliton becomes sharper, with injection strength. For the particular case of $\bar{u} = 0.8$, the solution to Eq. (26) predicts a boundary-layer width of ≈ 5. This is shown by the vertical solid green line in Fig. 2, in good agreement with both the numerical calculation and the analytical solution.

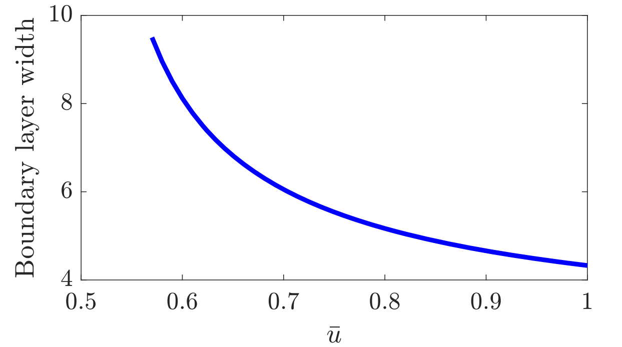

FIG. 4. Boundary-layer width as a function of the injection strength $\bar{u}$.

The boundary-layer width of Fig. 4 is presented in units of exchange length, valid for easy-plane anisotropy materials. For Permalloy with a typical exchange length of 5 nm, the boundary-layer width lies between 22 and 47 nm in a channel of 500 nm. For parameters associated with YIG [10], $A = 3.5$ pJ/m and $M_s = 130$ kA/m, the exchange length is ≈ 18 nm. This leads to a boundary-layer width between 78 and 172 nm in a channel of 1.8 μm.

IV. ELECTRICAL CIRCUIT ANALOGY

An alternative interpretation that captures the behavior of the channel subject to injection as a two-terminal device is the hydraulic analogy to electrical circuits. This analogy allows one to classify the DEFs and CS-DEFs in the context of electrical elements that provide building blocks to construct devices with a given functionality. For this, we define hydrodynamic quantities that are analogous to a voltage and a current, and from which the I-V characteristics of the device can be obtained.

In the electric to hydraulic analogy, a voltage maps to pressure difference. Using the hydrodynamic formulation of magnetization dynamics, the spatially dependent pressure $P(x)$ was derived in Ref. [3] as

$$2P(x) = [1 + n(x)^2][1 - |\mathbf{u}(x)|^2] - 1, \tag{27}$$

from which the pressure difference or voltage $V = P(x = L) - P(x = 0)$ in a channel of length L subject to BCs (6b) is

$$V = \tfrac{1}{2}\left[\left(n_L^2 - \bar{n}^2\right) + (1 + \bar{n}^2)\bar{u}^2\right], \tag{28}$$

where $n_L = n(x = L)$ and $\bar{n} = n(x = 0)$ are the densities at the channel's extrema.

The current I is equivalent to the density flux. In the steady-state modes studied here, the density flux is $(1 - n^2)\mathbf{u}$, whose magnitude corresponds to the precessional frequency, Eq. (3). Note that the precessional frequency is the only spatially homogeneous quantity of both DEFs and CS-DEFs, just as a current is an equilibrium, constant quantity in electric circuits.

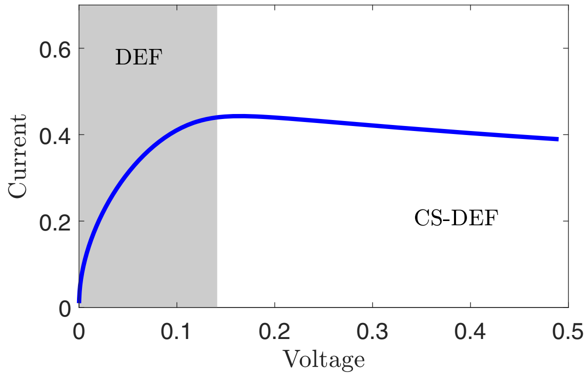

FIG. 5. I-V characteristics for a channel of length $L = 100$ and $\alpha = 0.01$ subject to a spin injection $\bar{u}$ at $x = 0$. The gray and white areas indicate the regions where, respectively, DEFs and CS-DEFs are sustained.

Additionally, in the case of a neighboring spin reservoir, the precessional frequency is linearly dependent on the pumped spin current that can give rise to a transverse charge current by the inverse spin-Hall effect [35].

Using Eqs. (28) and (3), we numerically calculate the I-V characteristics shown in Fig. 5 for a channel of length $L = 100$ and $\alpha = 0.01$. The gray and white areas indicate the sustenance of, respectively, a DEF or a CS-DEF. The I-V characteristic is nonlinear for all cases, and its finite value indicates that both DEFs and CS-DEFs are *resistive*. In other words, hydrodynamic states sustained in channels subject to spin injection can be classified as nonlinear resistors.

We note that in this representation, even the linear DEF solution Eq. (10) results in a nonlinear I-V curve. In fact, the linear solution establishes a spatially constant density, so that $n_L = \bar{n}$. Additionally, $|\bar{n}| \ll 1$, leading to a voltage given simply by $V = \bar{u}^2/2$. The precessional frequency is given in Eq. (10) so that $I = \bar{u}/(\alpha L)$. Therefore, the resistance is $R = V/I = \alpha L\bar{u}/2 = \alpha L\sqrt{V/2}$.

A notable feature of the I-V curve is the change in slope from positive when a DEF is sustained to negative when a CS-DEF is sustained. This agrees with the frequency tunability shown in Fig. 2(c). In terms of the differential conductivity, dI/dV, this implies a positive or negative sign for, respectively, DEFs and CS-DEFs. While the I-V characteristic is positive everywhere, the negative differential conductivity of CS-DEFs implies that these states can potentially amplify oscillatory inputs.

V. MICROMAGNETIC SIMULATIONS

In this section, we explore the DEF solutions established in a nanowire by micromagnetic simulations including both nonlocal dipole fields and magnetocrystalline anisotropy. We utilize the GPU-based code MUMAX3 [36]. We consider material parameters for Py, namely $M_s = 790$ kA/m, exchange stiffness $A = 10$ pJ/m, in-plane anisotropy field $H_A = 400$ A/m, and $\alpha = 0.01$. The corresponding exchange length for these parameters is $\lambda_{\rm ex} = 5.05$ nm.

We simulate a nanowire of dimensions 512 nm $\times$ 100 nm $\times$ 1 nm. Spin injection is achieved by STT acting on a 10 nm $\times$ 100 nm contact located at the left extremum of the nanowire. Therefore, the nanowire length subject to spin injection is 502 nm, which corresponds to a dimensionless length of $L = 99.4$. We use a symmetric STT with polarization $P = 0.65$ and assume that the charge current is spin-polarized along the $\hat{\mathbf{z}}$ direction, e.g., by a magnetic material with perpendicular magnetic anisotropy [37]. From a previous study [5], it was found that DEFs can be excited by STT in the presence of symmetry-breaking terms by charge-current densities on the order or 10^{11} A/m^2. We numerically find a threshold of $\bar{J} = 4 \times 10^{11}$ A/m^2. To explore the dynamical regimes discussed in Sec. III, we vary the charge-current density at the left contact, between 1×10^{11} A/m^2 and 20×10^{11} A/m^2 in steps of 1×10^{11} A/m^2. The simulation was set to run for 20 ns for each current, which was found to be sufficient to stabilize a steady-state regime.

The results can be visualized in the UHS phase space shown in Fig. 6(a). Because of the oscillations and transverse nonuniformity introduced by anisotropy and nonlocal dipole

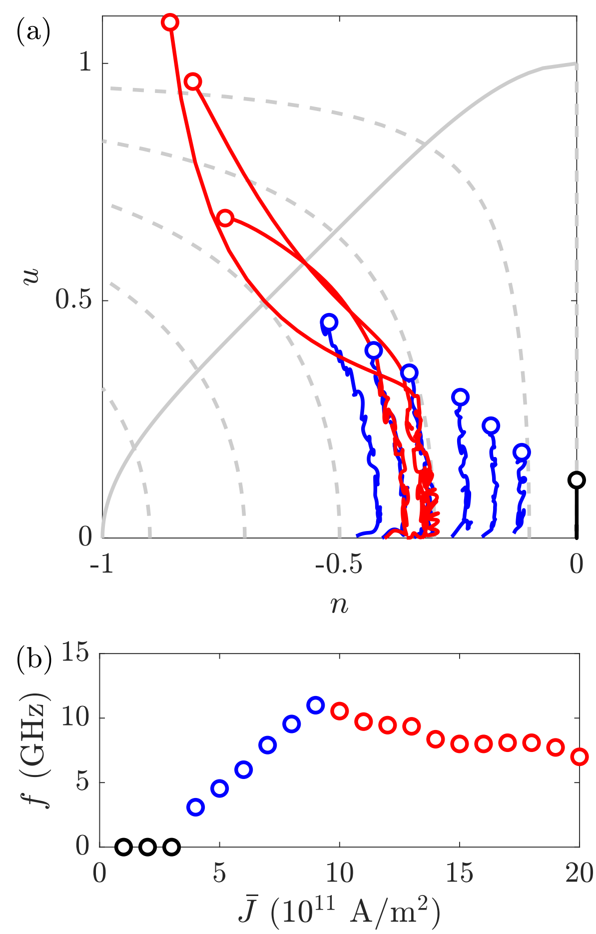

FIG. 6. (a) Magnetization states shown in the UHS phase space obtained from micromagnetic simulations of a Py nanowire of dimensions 512 nm $\times$ 100 nm $\times$ 1 nm subject to STT at the left extremum. The injection conditions are identified by circles and the corresponding solutions are plotted as solid curves. Subthreshold solutions are shown in black, DEFs in blue, and CS-DEFs in red. The solid and dashed gray curves represent the sonic curve and isofrequency contours for a UHS, respectively. (b) Frequency tunability as a function of $\bar{J}$.

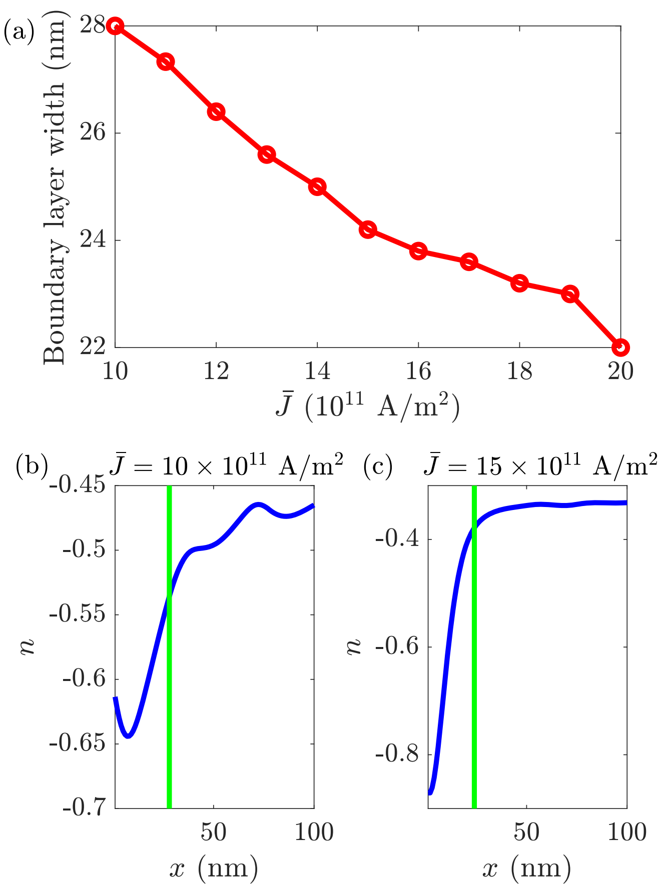

FIG. 7. Boundary-layer width as a function of the injection strength $\bar{u}$.

fields [5], respectively, we plot averaged densities and fluid velocities. The average is performed both in space across the width of the nanowire and in time for the range 15–20 ns. To directly compare with the analytical results, we disregard the region subject to STT. In other words, the boundary conditions are determined just outside the region subject to STT in the nanowire and the nanowire's right extremum. A current density threshold for the stabilization of hydrodynamic states is observed. At subthreshold current densities, a partial domain wall is formed at the injection site [5], evidenced by a solid black vertical line at $n = 0$.

We observe a remarkable qualitative agreement between the micromagnetic simulations and the analytical results shown in Fig. 3. In particular, we observe DEFs that follow the UHS isofrequency contours obtained in Sec. III without nonlocal dipole and in-plane anisotropy (solid blue curves) and CS-DEFs when the injection conditions are supersonic (solid red curves). Only three CS-DEFs are shown for clarity. The corresponding frequencies are shown in Fig. 6(b) in physical units as a function of $\bar{J}$ and color-coded as in panel (a). We emphasize that a linear relation between $\bar{J}$ and $\bar{u}$ is not possible to obtain because of the particularities of the energy landscape imposed by the magnetization texture, anisotropy, and nonlocal dipole fields. Nonetheless, a maximum frequency is observed at the transition between DEFs and CS-DEFs.

The boundary-layer width is difficult to calculate in micromagnetic simulations. This is because the frequency does not match exactly to the analytical results when nonlocal dipole and anisotropy fields are included, and, therefore, the determination of the parameter n_∞ is inaccurate. However, we can estimate the boundary-layer size from the spatial profile of n. We determine the boundary-layer width as the region in space where the slope of n is larger than a threshold value of 0.005 in units of $1/\lambda_{ex}$. In Fig. 7(a), we show the boundary-layer width as a function of injection current $\bar{J}$. The decreasing trend qualitatively agrees with the analytical results presented in Fig. 4, and the boundary-layer width is within the predicted values for Py. Because the criterion used for spin injection in micromagnetic simulations is different from the analytical boundary conditions, we show the profile of n close to the injection site for $\bar{J} = 10 \times 10^{11}$ A/m^2 and 15×10^{11} A/m^2 in Figs. 7(b) and 7(c), respectively. A reasonable estimation of the boundary-layer width, cf. Fig. 2, is observed.

VI. CONCLUSIONS

In this paper, we analytically determined the form and qualitative features of magnetization states sustained by spin injection of arbitrary strength in ferromagnetic channels with easy-plane anisotropy. For this, we utilize a dispersive hydrodynamic formulation that captures the necessary physical terms without approximations while being analytically tractable. Our analytical study fully characterizes the possible solutions that support long-distance spin transport under a unified framework.

We find that DEFs are generally nonlinear in profile and frequency tunability. Additionally, we characterize a novel solution, a CS-DEF, composed of a stationary soliton nucleated at the injection site that smoothly transitions into a nonlinear DEF. A notable consequence of the onset of CS-DEFs is that the frequency redshifts to injection. This feature is important for spintronic applications because it leads to a saturation of frequency and, therefore, of spin-current magnitudes pumped into adjacent spin reservoirs. It is numerically found that the maximum frequency monotonically decays with the channel's length, indicating the increased energy that must be invested in the nonlocal compensation of damping to sustain DEFs. In other words, there is a compromise between the spin-transport capacity and the length of the channel.

The adiabatic UHS interpretation introduced in this paper allows one to utilize the UHS phase space's isofrequency contours as a chart to categorize the magnetization states sustained in a ferromagnetic channel. This chart could be utilized to explore the profile of magnetization states induced in channels with two or more boundary conditions, e.g., contacts for STT and adjacent spin-current reservoirs [10]. The methodology presented here will be valuable for further analytical and numerical studies as well as to aid the design of an experimental realization of extended magnetization textures for microscopic spin transport.

ACKNOWLEDGMENTS

The authors thank T. J. Silva for helpful and insightful discussions. This material is based on work supported by the

U.S. Department of Energy, Office of Science, Office of Basic Energy Sciences under Award No. 0000231415. M.A.H. was partially supported by NSF CAREER DMS-1255422.

APPENDIX: ASYMPTOTIC ANALYSIS

In this Appendix, we implement an asymptotic analysis of the nonlinear ordinary differential equations (ODEs) (5a) and (5b) subject to the boundary conditions (6a) and (6b) that leads to the dissipative exchange flow regimes identified in this work: linear, nonlinear, and contact DEF solutions.

For this, we introduce the spatial rescaling

$$y = \frac{x}{L}, \tag{A1}$$

and we use Eq. (5a) to simplify Eq. (5b) and obtain the equivalent ODEs,

$$0 = [(1-n^2)u]' + \alpha L(1-n^2)\tilde{\Omega}, \tag{A2a}$$

$$\tilde{\Omega} = -(1-u^2)n + \frac{n''(1-n^2)+n(n')^2}{L^2(1-n^2)^2}, \tag{A2b}$$

where the prime denotes a spatial derivative with respect to y, $\tilde{\Omega} = \Omega/(1+\alpha^2)$ as before, and the boundary conditions (6) become

$$n'(0) = 0, \quad n'(1) = 0, \tag{A3a}$$

$$u(0) = \bar{u}, \quad u(1) = 0. \tag{A3b}$$

1. Linear DEF solution: Weak injection

The parameter regime that leads to the linear DEF solution requires sufficiently weak injection, therefore we introduce the small parameter $0 < |\bar{u}| \ll 1$ and the asymptotic expansions

$$u = \bar{u}u_1 + \bar{u}^3 u_3 + \cdots, \quad n = \bar{u}n_1 + \bar{u}^3 n_3 + \cdots,$$
$$\tilde{\Omega} = \bar{u}\tilde{\Omega}_1 + \bar{u}^3\tilde{\Omega}_3 + \cdots, \quad 0 < |\bar{u}| \ll 1. \tag{A4}$$

Inserting them into Eqs. (A2), and equating like powers of $\bar{u}$, we obtain the two equations

$$u_1' = -\alpha L\tilde{\Omega}_1, \tag{A5a}$$

$$\frac{1}{L^2}n_1'' - n_1 = \tilde{\Omega}_1, \tag{A5b}$$

at leading order $O(\bar{u})$. The boundary conditions (A3b) and Eq. (A5a) imply $u_1(y) = 1 - y$, $\tilde{\Omega}_1 = 1/(\alpha L)$. The boundary conditions (A3a) and Eq. (A5b) imply $n_1(y) = -1/(\alpha L)$. Inserting this approximate leading-order solution into the expansions (A4) yields the linear DEF solution (10).

We note that equating the next-order terms $O(\bar{u}^3)$ in Eqs. (A2) leads to

$$u_2' = \alpha L\big(n_1^2\tilde{\Omega}_1 - \tilde{\Omega}_2\big) + \big(n_1^2 u_1\big)', \tag{A6a}$$

$$\frac{1}{L^2}n_2'' - n_2 = \tilde{\Omega}_2 - u_1^2 n_1 - \frac{1}{L^2}n_1(n_1')^2. \tag{A6b}$$

Inserting the leading-order solution for n_1, u_1, and $\tilde{\Omega}_1$ into Eq. (A6a) results in $u_2' = -\alpha L\tilde{\Omega}_2$. Applying the boundary conditions (A3b) $[u_2(0) = u_2(1) = 0]$ implies $u_2(y) = 0$ and $\tilde{\Omega}_2 = 0$. Equation (A6b) and the boundary conditions (A3a) $[n_2'(0) = n_2'(1) = 0]$ are solved with a spatially varying $n_2(y)$ (superposition of exponentials and a quadratic polynomial in y). This means that the linear DEF solution (10) approximates the velocity and frequency to high accuracy, $O(\bar{u}^5)$, but the density has a spatially varying correction that scales with $\bar{u}^3$.

It is important to note that the linear DEF solution only requires sufficiently weak injection. Inspection of the asymptotic solution implies $0 < |\bar{u}| \ll \min(1, \alpha L)$ in order to maintain a well-ordered asymptotic series in the expansions (A4). Notably, there is no assumption on the magnitude of the damping coefficient α nor channel length L.

2. Nonlinear DEF solution: Long channel, subsonic injection

In this subsection, we provide the detailed derivation of Eqs. (13), (15), and (16). The assumption of weak injection for the linear DEF solution is relaxed, and now we require a long channel, i.e., $L \gg 1$. To this end, we assume the asymptotic expansions

$$u = u_0 + \frac{1}{L^2}u_2 + \cdots, \quad n = n_0 + \frac{1}{L^2}n_2 + \cdots,$$
$$\tilde{\Omega} = \tilde{\Omega}_0 + \frac{1}{L^2}\tilde{\Omega}_2 + \cdots, \quad L \gg 1, \tag{A7}$$

insert them into Eqs. (A2), and obtain the leading-order equations

$$0 = u_0' - \frac{2u_0 n_0 n_0'}{1-n_0^2} + \alpha L\tilde{\Omega}_0, \tag{A8}$$

$$\tilde{\Omega}_0 = -\big(1-u_0^2\big)n_0. \tag{A9}$$

Using Eq. (A9), we can eliminate n_0 from Eq. (A8) to obtain an ODE for u_0,

$$\alpha L\tilde{\Omega}_0 = u_0'\left[\frac{4\tilde{\Omega}_0^2 u_0^2}{\big(1-u_0^2\big)\big(u_0^4 - 2u_0^2 + 1 - \tilde{\Omega}_0^2\big)} - 1\right], \tag{A10}$$

which is equivalent to Eq. (12) in the main text. To integrate this expression, we perform partial fraction decomposition,

$$\alpha L\tilde{\Omega}_0 = u_0'\left[-1 + \frac{4}{u_0^2 - 1} - \frac{2(1-\tilde{\Omega}_0)}{u_0^2 - (1-\tilde{\Omega}_0)} - \frac{2(1+\tilde{\Omega}_0)}{u_0^2 - (1+\tilde{\Omega}_0)}\right]. \tag{A11}$$

This solution must agree with the linear DEF solution when $|\bar{u}|$ is small so, from Eq. (10), we expect $|\tilde{\Omega}_0| < 1$ and we can integrate each term in Eq. (A11) to obtain an implicit expression for $u_0(y)$,

$$\alpha L\tilde{\Omega}_0 y + C = -u_0 - 4\tanh^{-1}u_0 + 2\sqrt{1-\tilde{\Omega}_0}\tanh^{-1}\left(\frac{u_0}{\sqrt{1-\tilde{\Omega}_0}}\right) + 2\sqrt{1+\tilde{\Omega}_0}\tanh^{-1}\left(\frac{u_0}{\sqrt{1+\tilde{\Omega}_0}}\right), \tag{A12}$$

where C is an integration constant. Evaluating the boundary condition (A3b) $[u_0(1) = 0]$, we obtain the integration constant

$$C = -\alpha\tilde{\Omega}_0 L. \tag{A13}$$

Replacing C in Eq. (A12), we obtain the implicit solution for the fluid velocity that is given in the main text as Eq. (13). The frequency Ω_0 in Eq. (15) and density n_0 in Eq. (16) follow from the boundary condition $u_0(0) = \bar{u}$ and Eq. (A9), respectively.

This implicit solution satisfies the boundary conditions for the velocity (A3b) but it only satisfies $n_0'(1) = 0$ and not $n_0'(0) = 0$. While this could be resolved by considering a boundary layer adjacent to $y = 0$, the fact that we are considering a long channel implies $\frac{d}{dx}n_{\rm DEF}(0) = O(L^{-1})$, which is negligibly small within the asymptotic approximation (A7).

It is worth noting that the asymptotic expansion of the nonlinear DEF solution for small $|\bar{u}|$ is

$$u_{\rm DEF}(x) = \bar{u}\left(1 - \frac{x}{L}\right) + \bar{u}^5\frac{4\frac{x}{L}\left(1-\frac{x}{L}\right)}{3(\alpha L)^2}\left(\frac{x}{L} - 2\right) + O(\bar{u}^7), \tag{A14}$$

$$n_{\rm DEF}(x) = -\frac{\bar{u}}{\alpha L} - \bar{u}^3\frac{\left(1-\frac{x}{L}\right)^2}{\alpha L} + O(\bar{u}^5), \tag{A15}$$

$$\tilde{\Omega}_{\rm DEF} = \frac{\bar{u}}{\alpha L} - \frac{4\bar{u}^5}{3(\alpha L)^3} + O(\bar{u}^7), \tag{A16}$$

which agrees with the linear DEF solution at leading order and at $O(\bar{u}^3)$ for $L \gg 1$. A useful result is obtained by evaluating the nonlinear DEF solution at $x = 0$, which gives the relationship $n_{\rm DEF}(0) = -(\bar{u} + \bar{u}^3)/(\alpha L) + O(\bar{u}^5)$ between the spin density at the injection site and the injection velocity.

Although we have assumed $L \gg 1$, we have made no assumption on magnetic damping α. As noted in Sec. III D, the DEF frequency $\tilde{\Omega}$ saturates when injection achieves the local speed of sound [Eq. (24)]. This sets the maximum injection $\bar{u}$—which can still be relatively large—for the nonlinear DEF solution, i.e., injection must be *subsonic*.

3. CS-DEF solution: Weak damping, long channel, supersonic injection

To investigate the supersonic injection regime, we need to introduce a boundary layer near $y = 0$ in Eqs. (A2) (see, e.g., Ref. [33]). For this, we consider two separate solution regions: an inner region close to the injection site and an outer region that extends to the unforced edge of the channel. The solutions from these two regions are then asymptotically matched in order to obtain a uniformly valid asymptotic approximation across the entire channel.

a. Inner region

In the inner region, we are interested in the solution profile close to $y = 0$. Therefore, we “zoom” into this region for Eqs. (A2) by returning to the $x = yL$ scale (A1) where L is assumed large,

$$0 = [(1 - n^2)u]' + \alpha(1 - n^2)\tilde{\Omega}, \tag{A17a}$$

$$\tilde{\Omega} = -(1 - u^2)n + \frac{n''(1 - n^2) + n(n')^2}{(1 - n^2)^2}. \tag{A17b}$$

Now, the prime is a derivative with respect to x. As we will see, only the leftmost boundary conditions in (A3a) and (A3b) will be satisfied in the inner region. Anticipating the behavior of the solution in the outer region that we will match to, we use the following boundary conditions:

$$n'(0) = 0, \quad \lim_{x\to\infty} n'(x) = n_\infty, \tag{A18a}$$

$$u(0) = \bar{u}, \quad \lim_{x\to\infty} u(x) = u_\infty, \tag{A18b}$$

with n_∞ and u_∞ to be determined.

To approximately solve Eqs. (A17) subject to the boundary conditions (A18), we assume weak damping $0 < \alpha \ll 1$ and expand in the asymptotic series,

$$u = u_0 + \alpha u_1 + \cdots, \quad n = n_0 + \alpha n_1 + \cdots,$$
$$\tilde{\Omega} = \tilde{\Omega}_0 + \alpha\tilde{\Omega}_1 + \cdots, \quad 0 < \alpha \ll 1. \tag{A19}$$

This implies that in the inner region, the dynamics are effectively conservative to leading order,

$$0 = \left[\left(1 - n_0^2\right)u_0\right]', \tag{A20a}$$

$$\tilde{\Omega} = -\left(1 - u_0^2\right)n_0 + \frac{n_0''\left(1 - n_0^2\right) + n_0(n_0')^2}{\left(1 - n_0^2\right)^2}. \tag{A20b}$$

To continue, we integrate Eq. (A20a) to obtain u_0 in terms of n_0,

$$u_0 = \frac{C}{1 - n_0^2}, \tag{A21}$$

where C is a constant of integration. We substitute this into Eq. (A20b) and multiply by $2n'$ to obtain

$$2\tilde{\Omega}_0 n_0' + 2n_0 n_0' - C^2\left(\frac{1}{1 - n_0^2}\right)' = \left[\frac{1}{1 - n_0^2}\left(n_0'\right)^2\right]'. \tag{A22}$$

Every term in Eq. (A22) is a perfect derivative. Therefore, upon integration, we obtain the first-order ODE,

$$(n_0')^2 = -n_0^4 - 2\tilde{\Omega}_0 n_0^3 + (1 - K)n_0^2 + 2\tilde{\Omega}_0 n_0 - C^2 + K, \tag{A23}$$

where K is an additional constant of integration. This ODE can generally be integrated in terms of elliptic integrals (see, e.g., Ref. [34]), but we are interested in the localized, stationary soliton solution that satisfies the boundary conditions (A18), which is

$$n_{\rm in} = \frac{a\nu_1\tanh^2(\theta x) + \nu_2(n_\infty - a)}{a\tanh^2(\theta x) + \nu_2}, \tag{A24a}$$

$$u_{\rm in} = u_\infty\frac{1 - n_\infty^2}{1 - n_{in}^2}, \tag{A24b}$$

$$\tilde{\Omega}_{\rm in} = -n_\infty\left(1 - u_\infty^2\right), \tag{A24c}$$

where $\nu_1 = a - n_\infty - 2n_\infty u_\infty^2$, $\nu_2 = a - 2n_\infty - 2n_\infty u_\infty^2$, $\theta = \sqrt{1 - u_\infty^2 - n_\infty^2(1 + 3u_\infty^2)}$, and $a = n_\infty(1 + u_\infty^2) + \sqrt{(1 - u_\infty^2)(1 - n_\infty^2 u_\infty^2)}$. The soliton's density deviation from its far-field value n_∞ is the amplitude a. Note that the soliton's extremum is situated at $x = 0$ to enforce the BC $n'(0) = 0$. An additional relation is due to spin injection at the left boundary

$x = 0$ where the soliton's extremum is attained,

$$\bar{u} = u_{\rm in}(0) = u_\infty \frac{1 - n_\infty^2}{1 - (n_\infty - a)^2}. \tag{A25}$$

This relation constrains n_∞ and u_∞. We require an additional relation to fully determine the solution. This comes from the asymptotic solution in the outer region, far from the forced injection boundary at $x = 0$.

The soliton established in the inner region is therefore given by Eqs. (A24a), (A24b), and (A25), reported in the main text.

b. Outer region

For the outer region, we return to the scaled variable $y = x/L$ (A1) and Eqs. (A2). To match the inner solution (A24), we need to modify the boundary conditions (A2b) to

$$\lim_{y\to 0} n(y) = n_\infty, \quad n'(1) = 0, \tag{A26a}$$

$$\lim_{y\to 0} u(y) = u_\infty, \quad u(1) = 0. \tag{A26b}$$

The approximate outer solution to Eqs. (A2) subject to the boundary conditions (A26) is the nonlinear DEF solution described in Sec. A 2 with $L \gg 1$, $\bar{u} \to u_\infty$, which satisfies the following [cf. Eqs. (13), (15), and (16)]:

$$\alpha L \tilde{\Omega}_{\rm out}(1 - y) = u_{\rm out} + 4\tanh^{-1}(u_{\rm out}) - 2[\mathcal{N}^-(u_{\rm out}, \tilde{\Omega}_{\rm out}) + \mathcal{N}^+(u_{\rm out}, \tilde{\Omega}_{\rm out})], \tag{A27a}$$

$$n_{\rm out}(y) = -\frac{\tilde{\Omega}_{\rm out}}{1 - u_{\rm out}(y)^2}, \tag{A27b}$$

$$\alpha L \tilde{\Omega}_{\rm out} = u_\infty + 4\tanh^{-1}(u_\infty) - 2[\mathcal{N}^-(u_\infty, \tilde{\Omega}_{\rm out}) + \mathcal{N}^+(u_\infty, \tilde{\Omega}_{\rm out})]. \tag{A27c}$$

However, the boundary condition $n'(0) = 0$ no longer applies. Instead, we have a fixed value of the spin density

$$n_\infty = n_{\rm out}(0) = -\frac{\tilde{\Omega}_{\rm out}}{1 - u_\infty^2}. \tag{A28}$$

This relation and Eq. (A24c) imply the equality of the inner and outer precessional frequencies, so we define

$$\tilde{\Omega} = \tilde{\Omega}_{\rm in} = \tilde{\Omega}_{\rm out}. \tag{A29}$$

c. Matching

The full solution for the CS-DEF is obtained by matching the inner solution to the outer solution. Actually, the choice of boundary conditions in Eqs. (A18) and (A26) encodes the matching of the two solutions. We now summarize the three equations that uniquely determine n_∞, u_∞, and $\tilde{\Omega}$ in terms of the spin injection $\bar{u}$. They are

$$\tilde{\Omega} = -n_\infty(1 - u_\infty^2), \tag{A30a}$$

$$\bar{u} = \frac{u_\infty(1 - n_\infty^2)}{1 - (n_\infty - a)^2}, \tag{A30b}$$

$$\alpha L \tilde{\Omega} = u_\infty + 4\tanh^{-1}(u_\infty) - 2[\mathcal{N}^-(u_\infty, \tilde{\Omega}) + \mathcal{N}^+(u_\infty, \tilde{\Omega})], \tag{A30c}$$

coinciding with Eqs. (A24c), (A25), and (A27c), respectively.

With all parameters determined, we can now obtain a uniformly valid asymptotic approximation to the CS-DEF with

$$u_{\rm cs}(x) = u_{\rm in}(x) + u_{\rm out}(x/L) - u_\infty, \tag{A31a}$$

$$n_{\rm cs}(x) = n_{\rm in}(x) + n_{\rm out}(x/L) - n_\infty, \tag{A31b}$$

which is the approximation used, for example, in Fig. 2(b).

[1] E. B. Sonin, Spin currents and spin superfluidity, Adv. Phys. **59**, 181 (2010).
[2] S. Takei and Y. Tserkovnyak, Superfluid Spin Transport Through Easy-Plane Ferromagnetic Insulators, Phys. Rev. Lett. **112**, 227201 (2014).
[3] E. Iacocca, T. J. Silva, and M. A. Hoefer, Breaking of Galilean Invariance in the Hydrodynamic Formulation of Ferromagnetic Thin Films, Phys. Rev. Lett. **118**, 017203 (2017).
[4] E. Iacocca and M. A. Hoefer, Vortex-antivortex proliferation from an obstacle in thin film ferromagnets, Phys. Rev. B **95**, 134409 (2017).
[5] E. Iacocca, T. J. Silva, and M. A. Hoefer, Symmetry-broken dissipative exchange flows in thin-film ferromagnets with in-plane anisotropy, Phys. Rev. B **96**, 134434 (2017).
[6] D. Hill, S. K. Kim, and Y. Tserkovnyak, Spin-Torque-Biased Magnetic Strip: Nonequilibrium Phase Diagram and Relation to Long Josephson Junctions, Phys. Rev. Lett. **121**, 037202 (2018).
[7] S. Takei, B. I. Halperin, A. Yacoby, and Y. Tserkovnyak, Superfluid spin transport through antiferromagnetic insulators, Phys. Rev. B **90**, 094408 (2014).
[8] E. B. Sonin, Superfluid spin transport in ferro- and antiferromagnets, Phys. Rev. B **99**, 104423 (2019).
[9] P. Stepanov, S. Che, D. Shcherbakov, J. Yang, R. Chen, K. Thilahar, G. Voigt, M. W. Bockrath, D. Smirnov, K. Watanabe, T. Taniguchi, R. K. Lake, Y. Barlas, A. H. MacDonald, and C. N. Lau, Long-distance spin transport through a graphene quantum hall antiferromagnet, Nat. Phys. **14**, 907 (2018).
[10] T. Schneider, D. Hill, A. Kákay, K. Lenz, J. Lindner, J. Fassbender, P. Upadhyaya, Y. Liu, K. Wang, Y. Tserkovnyak, I. N. Krivorotov, and I. Barsukov, Self-stabilizing spin superfluid, arXiv:1811.09369.
[11] B. I. Halperin and P. C. Hohenberg, Hydrodynamic theory of spin waves, Phys. Rev. **188**, 898 (1969).
[12] J. König, M. C. Bønsager, and A. H. MacDonald, Dissipationless Spin Transport in Thin Film Ferromagnets, Phys. Rev. Lett. **87**, 187202 (2001).
[13] P. Bruno and V. K. Dugaev, Equilibrium spin currents and the magnetoelectric effect in magnetic nanostructures, Phys. Rev. B **72**, 241302(R) (2005).

[14] H. Chen, A. D. Kent, A. H. MacDonald, and I. Sodemann, Nonlocal transport mediated by spin supercurrents, Phys. Rev. B **90**, 220401(R) (2014).
[15] S. K. Kim, S. Takei, and Y. Tserkovnyak, Topological spin transport by Brownian diffusion of domain walls, Phys. Rev. B **92**, 220409(R) (2015).
[16] S. K. Kim, S. Takei, and Y. Tserkovnyak, Thermally activated phase slips in superfluid spin transport in magnetic wires, Phys. Rev. B **93**, 020402(R) (2016).
[17] Y. Liu, G. Yin, J. Zang, R. K. Lake, and Y. Barlas, Spin-Josephson effects in exchange coupled antiferromagnetic insulators, Phys. Rev. B **94**, 094434 (2016).
[18] P. Sprenger, M. A. Hoefer, and E. Iacocca, Magnonic band structure established by chiral spin-density waves in thin film ferromagnets, IEEE Magn. Lett. **10**, 4501605 (2019).
[19] T. L. Gilbert, A phenomenological theory of damping in ferromagnetic materials, IEEE Trans. Magn. **40**, 3443 (2004).
[20] Y. Tserkovnyak, A. Brataas, and G. E. W. Bauer, Enhanced Gilbert Damping in Thin Ferromagnetic Films, Phys. Rev. Lett. **88**, 117601 (2002).
[21] A. Qaiumzadeh, H. Skarsvåg, C. Holmqvist, and A. Brataas, Spin Superfluidity in Biaxial Antiferromagnetic Insulators, Phys. Rev. Lett. **118**, 137201 (2017).
[22] H. Ochoa, R. Zarzuela, and Y. Tserkovnyak, Spin hydrodynamics in amorphous magnets, Phys. Rev. B **98**, 054424 (2018).
[23] W. Yuan, Q. Zhu, T. Su, Y. Yao, W. Y. Xing, Y. Chen, Y. Ma, X. Lin, J. Shi, R. Shindou, X. C. Xie, and W. Han, Experimental signatures of spin superfluid ground state in canted antiferromagnet Cr_2O_3 via nonlocal spin transport, Sci. Adv. **4**, eaat1098 (2018).
[24] D. Stancil and A. Prabhakar, *Spin Waves: Theory and Applications* (Springer, Berlin, Germany, 2009).
[25] C. Liu, J. Chen, T. Liu, F. Heimbach, H. Yu, Y. Xiao, J. Hu, M. Liu, H. Chang, T. Stueckler, S. Tu, Y. Zhang, Y. Zhang, P. Gao, Z. Liao, D. Yu, K. Xia, N. Lei, W. Zhao, and M. Wu, Long-distance propagation of short-wavelength spin waves, Nat. Commun. **9**, 738 (2018).
[26] D. Wesenberg, T. Liu, D. Balzar, M. Wu, and B. L. Zink, Long-distance spin transport in a disordered magnetic insulator, Nat. Phys. **13**, 987 (2017).
[27] R. Lebrun, A. Ross, S. A. Bender, A. Qaiumzadeh, L. Baldrati, J. Cramer, A. Brataas, R. A. Duine, and M. Kläui, Tunable long-distance spin transport in crystalline antiferromagnetic iron oxide, Nature (London) **561**, 222 (2018).
[28] J. C. Slonczewski, Current-driven excitation of magnetic multilayers, J. Magn. Magn. Mater. **159**, L1 (1996).
[29] L. Berger, Emission of spin waves by a magnetic multilayer traversed by a current, Phys. Rev. B **54**, 9353 (1996).
[30] K. Avila, D. Moxey, A. de Lozar, M. Avila, D. Barkley, and B. Hof, The onset of turbulence in pipe flow, Science **333**, 192 (2011).
[31] S. K. Kim and Y. Tserkovnyak, Topological Effects on Quantum Phase Slips in Superfluid Spin Transport, Phys. Rev. Lett. **116**, 127201 (2016).
[32] V. E. Zakharov and L. A. Ostrovsky, Modulation instability: the beginning, Physica D **238**, 540 (2009).
[33] C. M. Bender and S. A. Orszag, *Advanced Mathematical Methods for Scientists and Engineers I: Asymptotic Methods and Perturbation Theory* (Springer-Verlag, Berlin, 1999).
[34] T. Congy, A. M. Kamchatnov, and N. Pavloff, Dispersive hydrodynamics of nonlinear polarization waves in two-component Bose-Einstein condensates, SciPost Phys. **1**, 006 (2016).
[35] A. Hoffmann, Spin Hall effects in metals, IEEE Trans. Magn. **49**, 5172 (2013).
[36] A. Vansteenkiste, J. Leliaert, M. Dvornik, M. Helsen, F. Garcia-Sanchez, and B. Van Waeyenberge, The design and verification of MUMAX3, AIP Adv. **4**, 107133 (2014).
[37] P. Bruno and J. P. Renard, Magnetic surface anisotropy of transition metal ultrathin films, Appl. Phys. A **49**, 499 (1989).